Inorganic Chemistry

Article

pubs.acs.org/IC

O′3−Na_xVO_2 System: A Superstructure for $Na_{1/2}VO_2$

Christophe Didier, Marie Guignard, Jacques Darriet, and Claude Delmas*

CNRS, Université de Bordeaux, ICMCB site de l'ENSCBP-IPB, 87 avenue du Dr. A. Schweitzer, Pessac, F-33608, France

Supporting Information

ABSTRACT: The electrochemical cycling in a sodium battery of the lamellar oxide $NaVO_2$ is reversible in the Na_xVO_2 composition range $1/2 \leq x \leq 1$. The complex electrochemical curve reveals the presence of several transitions taking place during deintercalation. With the help of in situ X-ray diffraction, we observed the structural transitions taking place between $Na_{2/3}VO_2$ and $Na_{1/2}VO_2$. The diffractograms show the presence of several monophasic domains separated by biphasic domains. All phases present a monoclinic distortion of the α-$NaFeO_2$ structure in the composition range $1/2 \leq x \leq 2/3$. Moreover the presence of a superstructure is evidenced for $Na_{1/2}VO_2$. It is the first time that an ordered structure is reported at the $Na_{1/2}MO_2$ composition with an O′3 oxygen stacking. A thorough investigation of electrochemically obtained O′3-$Na_{1/2}VO_2$ was performed. The structure refinement reveals the existence of a sodium/vacancy ordering, with a peculiar arrangement of the V−V distances hinting at a pairing of vanadium atoms. Our first measurements of the physical properties of O′3-$Na_{1/2}VO_2$ show a semiconductor behavior and a complex thermal dependence of the magnetic susceptibility related to the pairing of the vanadium atoms.

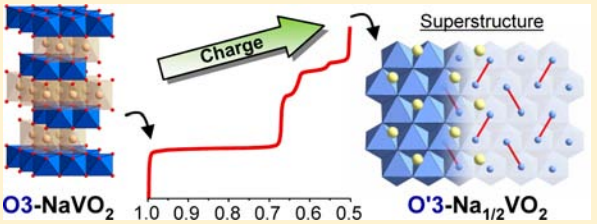

INTRODUCTION

Na_xMO_2 sodium layered oxides (M = 3d transition metal) are being revisited because of their potential use as electrode materials for Na-ion batteries[1−5] and also for their very interesting physical properties[6−8] even though most of them have been already known for 30 years.[9−15] Since the discovery of superconductivity at 5 K in P2−$Na_{\sim 0.35}CoO_2{\cdot}1.3\ H_2O$[7] and a high figure-of-merit for thermoelectricity in P2−$Na_{\sim 0.5}CoO_2$[16] the cobalt layered oxides are the most explored family.[17−21] Depending on the sodium amount in the interslab space, various types of oxygen packing (O3, P3, P2) can be obtained during the high temperature material synthesis.[22] For a given oxygen packing, the simultaneous minimization of the Na^+/Na^+ and $Na^+/M^{3+/4+}$ repulsions can lead to various sodium/vacancy orderings depending on the amount of sodium intercalated in the interslab space. These phenomena were intensively studied for the last ten years in the Na_xCoO_2 system.[23−28]

As the oxidation state of the transition metal in the $[MO_2]$ slab is determined by the amount of sodium in the interslab space, the physical properties can be tuned. A special focus has been drawn on P2−$Na_{1/2}CoO_2$ which exhibits a metal/insulator transition at 53 K.[28] A partial charge ordering of the $Co^{3+/4+}$ ions induced by the order of the Na^+ ions has been proposed[27−30] as an explanation of the origin of this transition, but it is still subject to discussions. This demonstrates the strong correlations existing between physical properties, structure organization and composition/electronic concentration. In this scope, new examples of Na_xMO_2 phases are required to better understand these relationships. We explored the homologous Na_xVO_2 system that is expected to present interesting structural and physical properties thanks to the specific d^1 and d^2 electronic configurations of V^{4+} and V^{3+}, respectively.

$NaVO_2$ was reported in the literature more than 30 years ago but was not obtained as a pure phase at this time.[12,31] It exhibits the classical α-$NaFeO_2$ (O3) layered structure (ABCABC oxygen stacking, Na^+ in octahedra) which was reported by Onoda who revisited this material.[8] The physical properties were studied by this author and also by Cava's group that unambiguously showed the existence of a low temperature orbital ordering[32] resulting from magnetic frustrations in the triangular lattice formed by the vanadium ions. This result was confirmed on theoretical grounds by various research groups.[33,34] It has also been shown by Onoda that for the $Na_{\sim 0.7}VO_2$ composition a P2 type structure (ABBA oxygen stacking, Na^+ in prisms) could be obtained.[8]

Since 2008, a general reinvestigation of the Na_xVO_2 system has been undertaken in our lab with two purposes: does this material present an interest as an electrode for sodium batteries and does it exhibit interesting structural and physical properties resulting from the peculiar electronic configuration of V^{3+} and V^{4+} ions? Some of us showed that the electrochemical intercalation (deintercalation) was a very elegant way to explore this system and to synthesize specific compositions by fixing the Fermi level vs Na^+/Na instead of using traditional solid-state chemistry.[20,35] By analogy to the electrochemical study performed on the Na_xCoO_2 system,[20] the deintercalation from O3−$NaVO_2$ and P2−$Na_{\sim 0.7}VO_2$ has been carried out. These two systems crystallize with different oxygen packings

Received: July 11, 2012
Published: September 25, 2012

   dx.doi.org/10.1021/ic301505e | *Inorg. Chem.* 2012, 51, 11007−11016

that cannot transform into each other without breaking V−O bonds.

The electrochemical study from O3−$NaVO_2$ allowed us to describe part of the three-layer Na_xVO_2 system. The galvanostatic cycling curve is shown in Figure 1. The

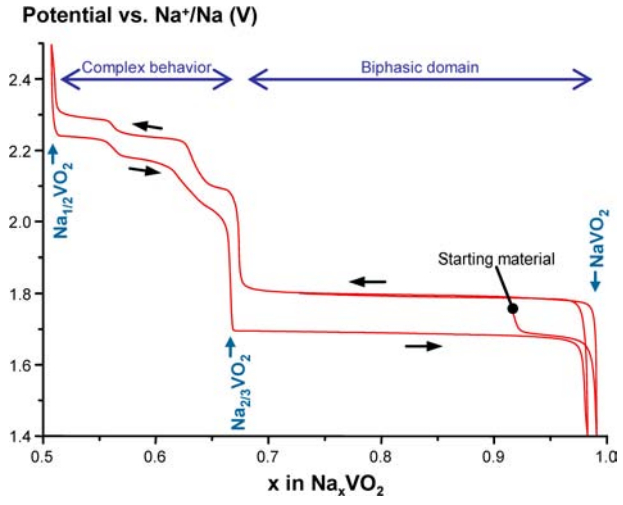

Figure 1. Galvanostatic cycling of O3−$NaVO_2$ in the composition range $1 \leq x \leq 1/2$ at rate $C/100$. The actual starting composition is $x \approx 0.92$ because of oxidation.[36] Special compositions are highlighted.

deintercalation/intercalation is completely reversible in the $1 \geq x \geq 1/2$ range; a large two phase domain is observed for $1 \geq x \geq 2/3$ and is followed by a complex domain between $2/3 \geq x \geq 1/2$.[36] This behavior was very recently confirmed by Hamani et al.[37] In our previous work, only the cell parameters were reported for the $Na_{1/2}VO_2$ and $Na_{2/3}VO_2$ compositions which revealed an O′3 structure (ABCABC oxygen stacking with a monoclinic distortion, Na^+ in octahedra).[36] This structure is different from the one obtained by chemical deintercalation up to the $Na_{\sim 0.6}VO_2$ composition followed by a thermal treatment at 200 °C, which presents the P′3 structure (AABBCC stacking with a monoclinic distortion, Na^+ in trigonal prisms) with a modulation vector along b*.[38]

In this work, we electrochemically removed sodium from O3−$NaVO_2$ and performed in situ X-ray diffraction during the deintercalation. This technique allows a continuous observation of the Na_xVO_2 composition domain while simultaneously observing structural changes and the correlation with the oxidation potential (Fermi level) of the material. We then focused on the structural determination of O′3−$Na_{1/2}VO_2$ for which we found a Na^+/vacancy ordering within the interslab space leading to a superstructure. First measurements of the physical properties have been undertaken.

EXPERIMENTAL SECTION

$NaVO_2$ is obtained by reduction of $NaVO_3$ under H_2 as described in our previous work.[36] Because of its very reducing character, there is always formation of a small amount of the $Na_{2/3}VO_2$ phase. A battery with the following electrochemical chain: Na metal | $NaClO_4$ (1M) in propylene carbonate | $NaVO_2$ mixed with graphite/carbon black and PTFE (polytetrafluoroethylene) as a binder (mass ratios 88:10:2), was assembled within an argon-filled glovebox in a homemade cell for in situ measurements. The positive electrode material is placed against a beryllium current collector. We used glass microfiber filters (1.2 μm pore size) as separators. During the in situ measurement, the cell was charged intermittently for 45 min at rate $C/100$ (1 e^- per formula unit (FU) transferred in 100 h) with 3 h 30 min relaxation at each step, using a Biologic VMP potentiostat. X-ray diffraction (XRD) acquisitions were made during the relaxations, when the cell voltage was almost constant, using a Panalytical X'pert diffractometer (Bragg−Brentano geometry) operating with Cu−$K_{\alpha 1}$ radiation (λ = 1.5406 Å) in the $25° \leq 2\theta \leq 45°$ range (0.017°/6s per step).

The O′3−$Na_{1/2}VO_2$ phase has been synthesized in Swagelok-type batteries using the potentiostatic method described in our previous study of the Na_xCoO_2 system.[20] The electrochemical chain is the same except no PTFE was added to the mixture of $NaVO_2$ and graphite. The absence of binder allows a sample preparation for X-ray diffraction with less preferential orientation of the crystallites. In our previous electrochemical study we showed that around the $x \approx 1/2$ composition there is a rapid potential increase from 2.30 to 2.60 V. Therefore, we assumed that 2.45 V versus Na^+/Na corresponds to the Fermi level of this phase in this potential scale. The cell was first charged galvanostatically at a $C/100$ rate up to 2.45 V, after which the potential was maintained at this value. During this potentiostatic step, the current slowly drops down to 0 A as the material reaches its equilibrium state. Depending on the amount of material, this step can take up to 2 weeks. The experiment was performed at room-temperature with a Biologic VMP3 potentiostat.

The powder is then recovered in a glovebox, washed with dimethylcarbonate and then dried under vacuum. The powder XRD acquisitions were done under dynamic vacuum ($<10^{-4}$ mbar, aluminized Kapton window) and recorded using a Panalytical X'pert diffractometer (Bragg−Brentano geometry) with Cu−K_α radiation (λ_1 = 1.5406 Å and λ_2 = 1.5444 Å) in the range $10° \leq 2\theta \leq 130°$ (0.02°/5s per step). Acquisitions were made for T = 300 and 10 K. The Rietveld refinement of the XRD data was done with *Jana2006* software.[39] The background was estimated by a Legendre function and peak shapes were described by a pseudo-Voigt function.[40] The region where graphite is visible was excluded. The composition $Na_{1/2}VO_2$ was confirmed by ICP-AES measurements, after dissolving the sample in hot aqua regia; the measured Na/V ratio is close to ∼0.5.

Neutron diffraction (ND) data were collected at Laboratoire Léon Brillouin (Saclay, France) using the high-resolution diffractometer 3T2 (λ = 1.225 Å) at room-temperature in the range $10° \leq 2\theta \leq 120°$ (0.05° per step). For magnetic structure determinations, the G41 diffractometer (λ = 2.423 Å) was used in the range $5° \leq 2\theta \leq 80°$ (0.02° per step) with acquisitions at 298, 200, 100, and 2 K. The samples were contained in airtight cylindrical vanadium sample holders.

Resistivity measurements should ideally be made on sintered samples without graphite, however $Na_{1/2}VO_2$ cannot be sintered as it transforms irreversibly into a P′3 phase[38] at ∼370 K. Thus pellets of $NaVO_2$ without graphite were first sintered at 600 °C for 48 h in a sealed gold tube, before applying on the pellet the potentiostatic method previously described to reach the $Na_{1/2}VO_2$ composition. The resistivity is then measured in an airtight apparatus, with the four-probe technique using a direct current, between room temperature and 50 K (cooling and warming). Magnetic measurements were made with a SQUID magnetometer (Quantum Design) on ∼50 mg of powder from a ground pellet with no graphite. The magnetic susceptibility was measured in an applied field of 1 kOe, at temperatures ranging between 2 and 350 K (ZFC/FC). A correction for the diamagnetic contributions was applied using Pascal's constants.[41] Field induced magnetization was measured at various temperatures between −50 and 50 kOe. Heat capacity measurements were done with a PPMS apparatus (Quantum Design) on part of a pellet of O′3−$Na_{1/2}VO_2$ in the 2−250 K temperature-range.

RESULTS AND DISCUSSION

In Situ X-ray Diffraction. To have a better understanding of the transitions taking place during sodium deintercalation from O3−$NaVO_2$ (Figure 1), we have investigated the deintercalation process by in situ XRD during the charge of the battery. The cell was first continuously charged at the $C/100$ rate to the "$Na_{\sim 0.72}VO_2$" average composition, close to the end of the two phase plateau. Then an alternation of charges

dx.doi.org/10.1021/ic301505e | *Inorg. Chem.* 2012, 51, 11007−11016

and relaxations was applied, with a XRD data acquisition during each relaxation step, when the electrode material was at a pseudo steady-state.

The evolution of the XRD pattern with the sodium amount is represented in Figure 2. For the "$Na_{\sim 0.72}VO_2$" average composition, peaks of O3−$NaVO_2$ are clearly visible. The intensity of these diffraction peaks decreases continuously until the $Na_{2/3}VO_2$ composition. A small contribution of $NaVO_2$ remains present even for sodium compositions lower than $x = 2/3$, and is attributed to electrochemically inactive powder lost in the separators, as can be seen during the recovery. This phenomenon is also observed in ex situ experiments due to the cell preparation which is currently not fully optimized. The major diffraction peaks can be indexed in the monoclinic system that we defined for the O′3 type.[36] For all phases, the space-group is $C2/m$ and the unit cell parameters are close to $a \approx 5.0$ Å, $b \approx 2.9$ Å, $c \approx 6.6$ Å, $\beta \approx 121°$.

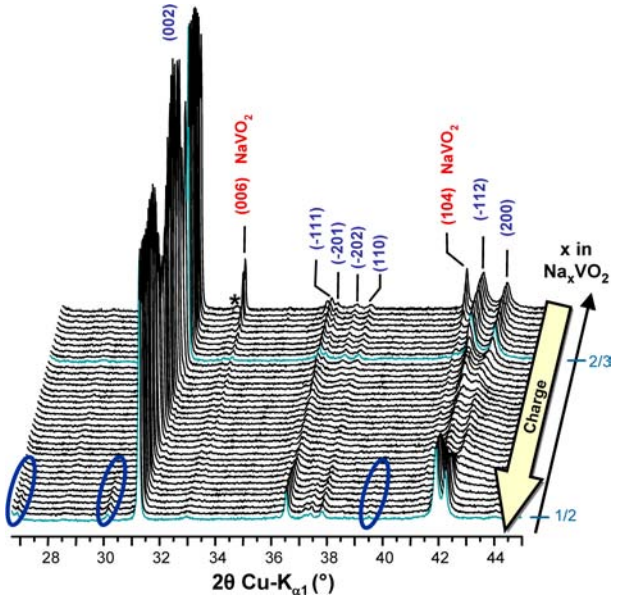

Figure 2. In situ powder XRD diagram obtained during the deintercalation of O3−$NaVO_2$. The first X-ray acquisition starts at $x \approx 0.72$. Indexations are of the O′3 monoclinic cell, unless indicated otherwise. Some of the indexations of the O3−$NaVO_2$ hexagonal cell are also indicated. The asterisk shows a small impurity of V_2O_3 which was already present in the starting $NaVO_2$ phase. Circles highlight the onset of superstructure peaks when approaching the $Na_{1/2}VO_2$ composition.

The displacement of the peaks emphasizes the cell parameter changes in the $0.67 \geq x \geq 0.50$ composition range. An enlargement of the most intense peaks is given in Figure 3. The electrochemical curve is reported for comparison. One can note a very good correlation between the electrochemical curve and the structural changes. The shift of the (002) diffraction peak is closely related to the variations of the electrochemical voltage. In the monoclinic O′3 structure, the position of the (002) peak is characteristic of the interslab distance ($2d_{002} = c \sin \beta$); the shift of this peak toward lower 2θ values as sodium is removed shows the gradual increase of the interslab distance due to increasing oxygen repulsions as the amount of sodium ions in the interslab decreases.

In the $0.67 > x > 0.64$ composition range, the position of the diffraction peaks changes continuously; this can suggest a solid solution behavior. Nevertheless in this hypothesis no broadening of the peaks would be expected; here the (002) peak broadens at mid composition. One can assume that the peak broadening results from the existence of a biphasic domain with very close cell parameters for the two phases. Also the coherence length must be smaller since all of these phase transitions occur within each crystallite due to their topotactic

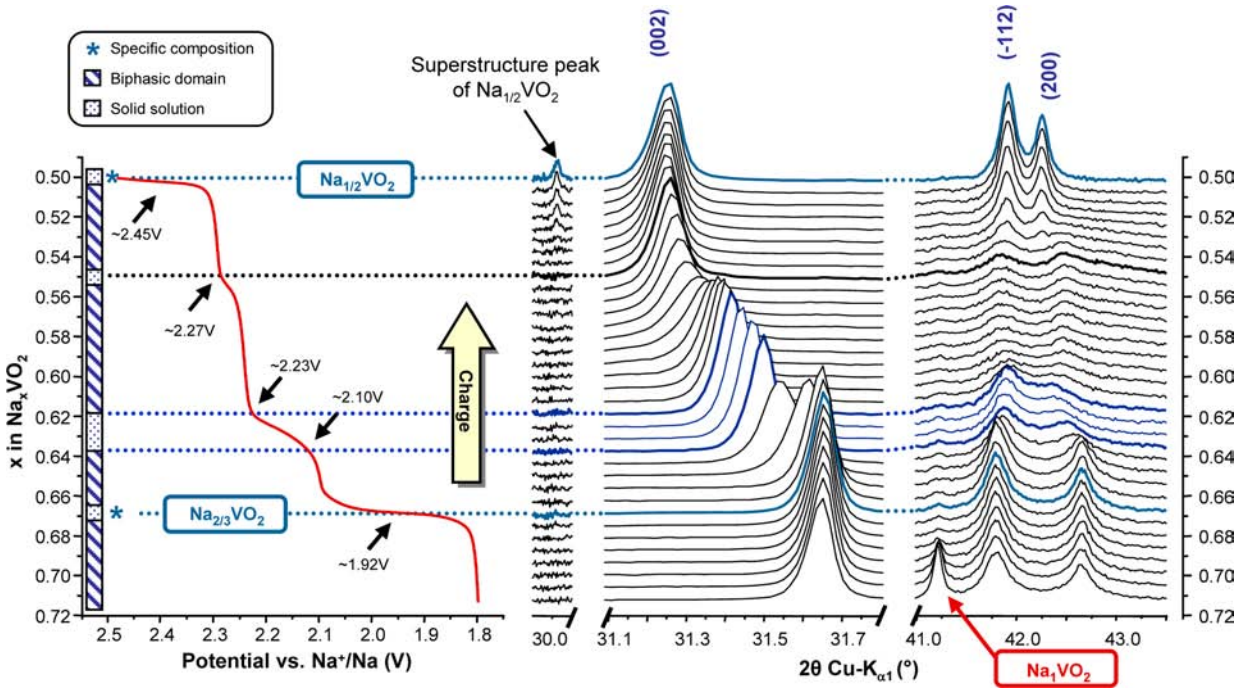

Figure 3. Zoom over the (002), (−112) and (200) peaks as indexed in the O′3 monoclinic cell from the patterns measured during the deintercalation of O3−$NaVO_2$. The diffractograms are aligned to the electrochemical curve of a galvanostatic charge (obtained in an ex situ battery). A crude phase diagram of the transitions deduced from the XRD patterns and electrochemical curve is included.

dx.doi.org/10.1021/ic301505e | Inorg. Chem. 2012, 51, 11007−11016

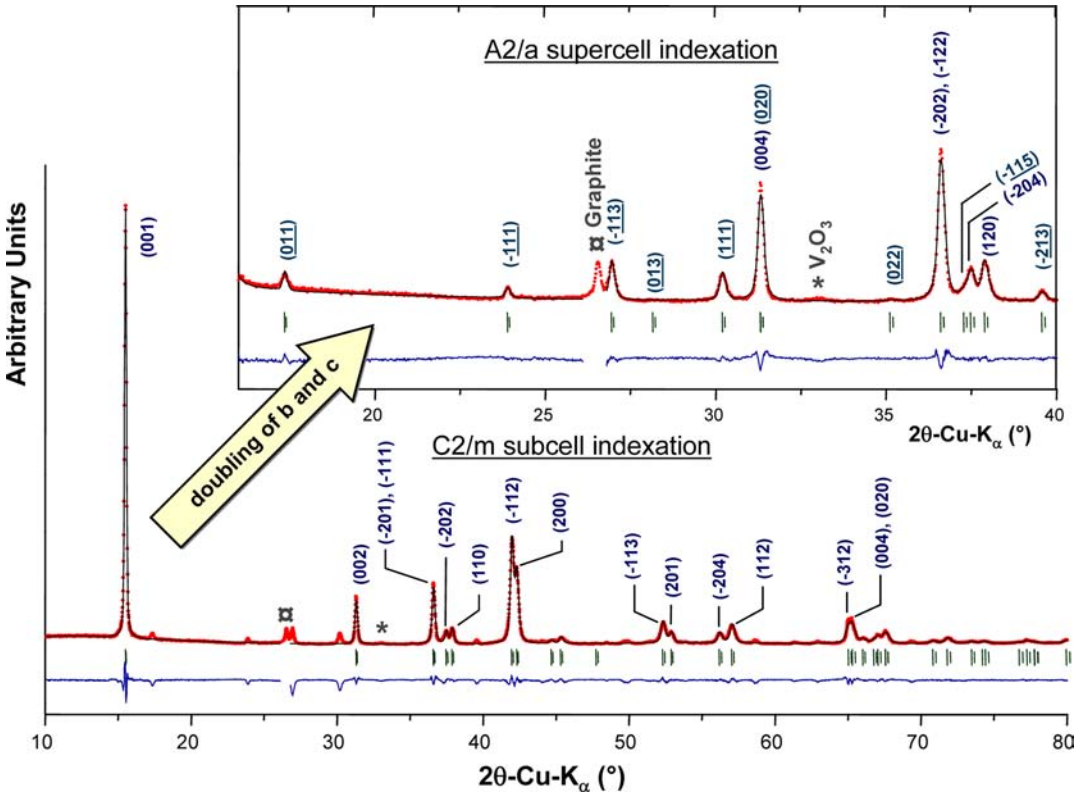

Figure 4. Profile matching of the powder XRD pattern of O′3−$Na_{1/2}VO_2$ using the *C*2/*m* subcell. The insert shows the indexation when *b* and *c* parameters are doubled and the space-group is *A*2/*a*. Superstructure peaks indexations are underlined.

character, hence the peak broadening. A similar observation can be made for the plateau between $0.62 > x > 0.55$. The plateau observed at $0.55 > x > 0.50$ is characteristic of a biphasic domain, as shown by the gradual change of the superstructure peaks intensities.

The pattern appears to be monophasic for x between 0.64 and 0.62, with a progressive evolution of the unit cell parameters (Figure 3). This corresponds to a solid solution domain. The displacement of the (002) peak without change of its FWHM value is characteristic of this behavior. Even though a clear trend of d_{002} can be seen, the *c* and β parameters can change in opposite directions making it difficult to fit unit cell parameters; thus we found very close unit cell parameters for each of the scans, however the data precision does not allow us to find a significant trend in the parameters. We report here the cell parameters found for *x* close to 0.63: $a = 4.950(6)$ Å, $b = 2.864(3)$ Å, $c = 6.605(7)$ Å, and $\beta = 120.80(10)°$. Single phases are observed for $Na_{2/3}VO_2$ and $Na_{1/2}VO_2$ compositions, with unit cell parameters as previously reported.[36] Extra peaks ($2\theta \approx 26.7°$ and 30.0°) close to $x = 0.50$ are not indexed in the monoclinic cell (Figure 2). These additional peaks suggest a supercell for $Na_{1/2}VO_2$ that we discuss in the next part.

The resulting phase diagram for the deintercalation of $NaVO_2$ is shown in Figure 3. The large voltage variations on the electrochemical curve around 1.92 and 2.45 V are characteristic of single phases with specific composition $Na_{2/3}VO_2$ and $Na_{1/2}VO_2$ respectively, while the smoother variation between 2.10 and 2.23 V coincides with a solid solution domain. The small voltage bump at 2.27 V might correspond to a single phase of composition $Na_{\sim 0.55}VO_2$, however there is also a significant broadening of the (−112) and (200) peaks. This reveals a certain disorder of the structure at this composition. These various monophasic domains are separated by biphasic domains leading to plateaus on the electrochemical curve. This shows again the good correlation between the electrochemical curve and the structural changes occurring during deintercalation.

Structure of O′3−$Na_{1/2}VO_2$. The O′3−$Na_{1/2}VO_2$ phase was obtained either in powder (with graphite) or in sintered pellets (without graphite) by the potentiostatic method described in the Experimental Section. The indexation of the main peaks up to $2\theta = 80°$ from the powder XRD pattern obtained at room-temperature is given in Figure 4. They are indexed with a monoclinic cell (*C*2/*m*) with parameters: $a = 4.972(2)$ Å, $b = 2.8554(7)$ Å, $c = 6.650(3)$ Å, and $\beta = 120.82(2)°$. The main peak of graphite (added during electrode manufacturing) as well as a very weak peak of the impurity V_2O_3 (observed in the starting $NaVO_2$ phase) are also visible (Figure 4). However extra diffraction peaks remain unindexed. It is in fact possible to index these peaks considering a supercell with parameters *b* and *c* being the double of those of the subcell (insert Figure 4). All the peaks would then satisfy extinction conditions of the space-group *A*2/*a*. For the unit cell to have a standard space-group (*C*2/*c*), the *a* and *c* unit cell parameters were permuted. The transformation from the original subcell to the supercell we used is given by

$$\vec{a}_{\text{supercell}} = 2\vec{c}_{\text{subcell}}$$

$$\vec{b}_{\text{supercell}} = -2\vec{b}_{\text{subcell}}$$

$$\vec{c}_{\text{supercell}} = \vec{a}_{\text{subcell}}$$

dx.doi.org/10.1021/ic301505e | *Inorg. Chem.* 2012, 51, 11007−11016

As a result all peaks are indexed in the supercell ($C2/c$ space-group) with unit cell parameters: a = 13.299(2) Å, b = 5.7104(6) Å, c = 4.9713(6) Å, and β = 120.824(9)°.

The atomic position of the vanadium atoms was determined using the charge flipping program *Superflip* included in the *Jana2006* software,[42] with starting composition $Na_{1/2}VO_2$ (Z = 8). The algorithm found the vanadium atom to occupy a *8f* position (x, y, z) with $x \approx 0.25$, $y \approx 0.37$, and $z \approx 0.22$. The position of other atoms was deduced from Fourier difference maps. Two *8f* positions distanced ~2 Å away from the V position were found: $x \approx 0.36$, $y \approx 0.13$, $z \approx 0.25$ assigned to O1 and $x \approx 0.15$, $y \approx 0.12$, $z \approx 0.20$ assigned to O2. A new Fourier difference allowed us to localize the sodium ions. The sodium atoms can occupy two *4e* positions (0, y, 1/4) distanced ~2.3 Å away from the oxygen positions: $y \approx 0.35$ assigned to Na1 and $y \approx 0.86$ assigned to Na2.

A full occupancy of these two positions corresponds to a Na_1VO_2 composition. Thus two possibilities of distribution for the sodium atoms can be assumed in order to satisfy the experimental composition $Na_{1/2}VO_2$: a statistical repartition of the sodium atoms on both sites (each site 50% occupied) or a perfect ordering with one site fully occupied and the other one empty. When a statistical occupation of the sodium sites is chosen (Figure 5a), the peaks corresponding to the doubling of the unit cell parameters are not well fitted by the calculated profile compared to the case where only one sodium site is occupied (Figure 5b). Thus there is an ordering of the sodium atoms within the interslab which is at the origin of the superstructure. The occupation of either sodium site (Na1 or Na2) leads to the same structure after refinement, with a different position of the origin of the unit cell.

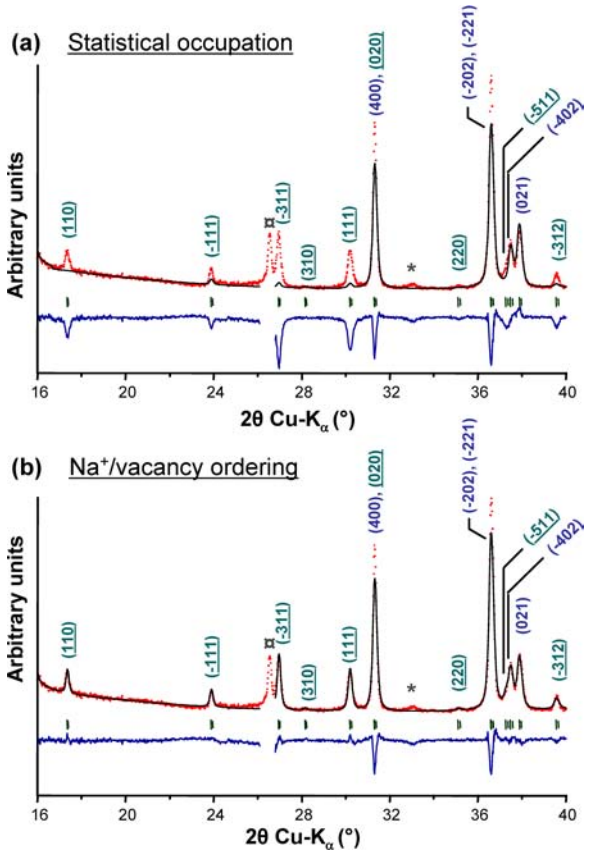

Figure 5. Structure refinement of O′3–$Na_{1/2}VO_2$ (a) with a statistical occupation of the sodium sites (50% in each site) or (b) with only one sodium site occupied. The indexation in the $C2/c$ supercell is reminded. Superstructure peaks are badly fitted in the first hypothesis. Visible impurities are also indicated (¤ for graphite and * for V_2O_3).

The full profile of the Rietveld refinement up to 2θ = 130° is given in Figure 6. The isotropic displacement parameters (B_{iso}) of O1 and O2 were chosen to be equal and a correction for roughness absorption of pulverized samples in the Bragg–Brentano geometry[43] was introduced into the refinement. The structure refinement results, refined atomic positions and B_{iso} are gathered in Table 1. Interatomic distances are listed in Table 2. Perspective views of the layered structure are given in Figure 7.

The main feature of the structure is the sodium/vacancy ordering in the interslab space, as shown in Figure 8a. One can see that sodium ions are strongly displaced from the center of the octahedral sites, with four short and two long Na–O distances (Table 2). This is probably a consequence of Na^+/Na^+ repulsions as it further increases the distance between Na^+ ions. The bond valence sum (BVS) of Na^+ is equal to 1.07(2), in agreement with the expected value.

The lowering of the crystal symmetry from rhombohedral (O3 structure) to monoclinic (O′3 structure) allows for strong deformations of the triangular network of vanadium layers. A slight rippling of the [VO_2] slabs is visible (Figure 7b) in the b direction. The vanadium ions are also slightly displaced from the center of the octahedra, with V–O distances ranging from 1.92 Å to 2.09 Å (Table 2). These distortions lead to the existence of a peculiar distribution of short and long V–V distances (Table 2), as illustrated in Figure 8b. There is formation of vanadium pairs with very short V–V distances (2.64 Å) while other distances are significantly larger (from 2.86 Å to 3.00 Å). The value of this short distance is close to the one found in other vanadium oxides (2.62 Å in VO_2,[44] 2.69 Å in V_5O_9,[45] 2.69 Å in V_4O_7,[46] 2.70 Å in V_2O_3[47]), which also exhibit a pairing of vanadium ions. The BVS of vanadium ions is 3.55(8), which is in agreement with a formal mixing of 0.5 V^{3+} and 0.5 V^{4+} in $Na_{1/2}VO_2$. There is only one vanadium site, therefore no long-range ordering of V^{3+} and V^{4+} could be evidenced from our observations.

The distribution of Na^+ ions and vacancies in the interslab is related to the organization of the V–V distances within the [VO_2] slabs. This is highlighted in Figure 8b, which shows that vacancies on each side of the [VO_2] slabs are closer to the shortest V–V distances; inversely sodium ions face the longest V–V distances. This is probably a result of the minimization of the $V^{3+/4+}$/Na^+ electrostatic repulsions.

In relation to the physical property study presented further, X-ray and neutron diffraction studies have been performed at low temperatures. XRD measurements did not reveal any structural transition from room-temperature down to 10 K, apart from a slight contraction of the unit cell: a = 13.224(2) Å, b = 5.6894(6) Å, c = 4.9539(7) Å, and β = 120.592(11)°. This contraction is anisotropic due to the bidimensional nature of the structure, as was already observed in P2–$Na_{1/2}CoO_2$.[27] The Rietveld refinement at 10 K leads to very similar results that confirm the structure and show that the V–V pairing (2.62 Å at 10 K) is still present at lower temperatures. Tables of refined atomic parameters and interatomic distances at 10 K are included in Supporting Information Table S1 and Table S2, respectively. The Rietveld refinement of the ND pattern confirms the structure determined from XRD. No extra peak

dx.doi.org/10.1021/ic301505e | *Inorg. Chem.* 2012, 51, 11007–11016

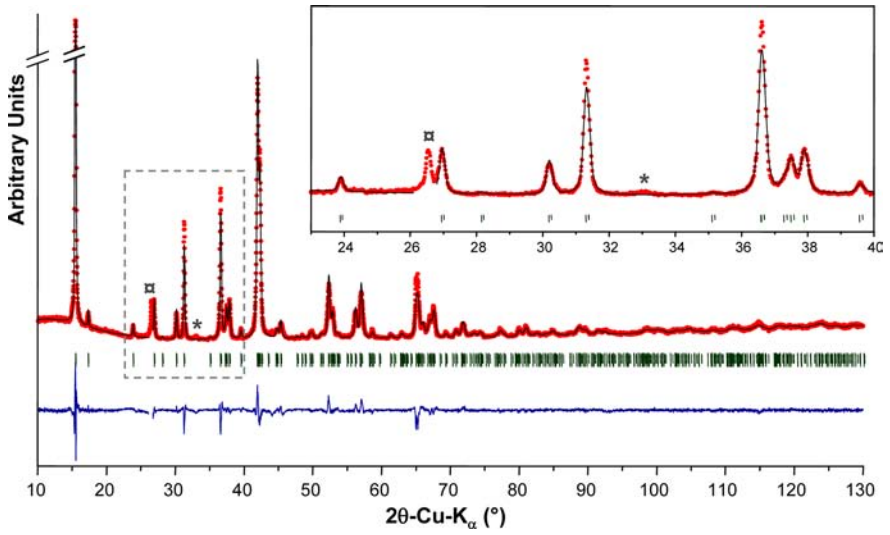

Figure 6. Rietveld refinement of the powder XRD pattern of O′3−$Na_{1/2}VO_2$ obtained by the potentiostatic method. Detected impurities are indicated (¤ for graphite and * for V_2O_3). The inset shows a zoom over the 23°−40° region.

Table 1. Structural Parameters in O′3−$Na_{1/2}VO_2$ at Room-Temperature[a]

atom type	Wyckoff	*x*	*y*	*z*	B_{iso} (Å^2)
V	8*f*	0.2487(6)	0.3666(11)	0.2276(13)	0.9(2)
O1	8*f*	0.3522(14)	0.124(3)	0.222(4)	1.0(2)
O2	8*f*	0.1614(13)	0.128(3)	0.291(4)	1.0(2)
Na	4*e*	0	0.301(2)	1/4	1.2(5)

[a]The space-group is *C*2/*c* (*Z* = 8) and the unit cell parameters: *a* = 13.299(2) Å, *b* = 5.7104(6) Å, *c* = 4.9713(6) Å, and *β* = 120.824(9)°. The agreement factors of the refinement are R_p = 6.7%, R_{wp} = 9.0%, R_{exp} = 5.9%, GOF = 1.53.

resulting from a long-range magnetic ordering is visible from room-temperature to 2 K (Supporting Information Figure S3).

Electrical and Magnetic Properties of O′3−$Na_{1/2}VO_2$. Electrical resistivity measurements, performed on a pellet of O′3−$Na_{1/2}VO_2$ in the 50 K−300 K range, are displayed in Figure 9a. The resistivity *ρ* shows a reversible semiconductor temperature dependence with *ρ* increasing from ∼10^1 Ω.cm at 300 K to ∼10^7 Ω.cm at 100 K. Resistivity at lower temperatures was too high for our measuring device and thus is not reported here. No anomaly of the conductivity is observed in this temperature range, which is in agreement with the low temperature XRD measurements that did not show any structural transition.

Figure 9b shows the variations of $\ln(\sigma)$ versus T^{-1} (Arrhenius plot). At high temperatures, a linear variation is observed corresponding to $\sigma_0 \approx 9.2 \times 10^2$ S/cm and $E_a \approx 0.23$ eV, which is in agreement with values usually observed for a hopping conduction mechanism. However a significant discrepancy is observed at lower temperatures. Therefore, we have considered Mott's variable range hopping (VRH) conduction mechanism of the conductivity defined by the equation[48,49]

$$\sigma = A \times \exp\left[-\left(\frac{T_0}{T}\right)^{1/4}\right]$$

where *A* and T_0 are constants. As shown in Figure 9c, the curve of $\ln(\sigma)$ versus $T^{-1/4}$ is fairly linear for $T < 250$ K, with $A \approx 2.3 \times 10^{18}$ S/cm and $T_0 \approx 1.2 \times 10^9$ K. This VRH behavior might be related to a localization of the electrons due to the V−V pairing and the distribution of V−V distances, as represented in Figure 8b; however additional transport property measurements are required in order to understand the interactions at the origin of this behavior.

The thermal variation of the magnetic susceptibility *χ* is given in Figure 10. No difference is observed between the FC and ZFC curves. No opening of a hysteretic cycle is apparent on the magnetization versus field measurements (inset Figure 10). At $T = 2$ K and for high magnetic field values, the magnetization is weak and almost constant which could be the signature of strong antiferromagnetic exchange interactions. The variation of the specific heat in the temperature range 2−250 K (Figure 11) does not show any *λ*-anomaly characteristic of a 3D long-range magnetic ordering in agreement with neutron diffraction measurements that did not reveal the presence of magnetic diffraction peaks from room-temperature down to 2 K (Supporting Information Figure S3).

Table 2. Interatomic Distances in O′3−$Na_{1/2}VO_2$ at Room Temperature

distance (Å)		distance (Å)		distance (Å)	
V−V	1× 2.641(10)	V−O2	1× 1.92(2)	Na−O2	2× 2.28(2)
V−V	2× 2.863(9)	V−O1	1× 1.931(16)	Na−O1	2× 2.377(14)
V−V	2× 2.916(10)	V−O2	1× 1.94(2)	Na−O1	2× 2.65(2)
V−V	1× 3.002(11)	V−O1	1× 1.96(2)	Na−Na	2× 3.367(12)
		V−O2	1× 2.055(17)	Na−Na	2× 4.243(14)
		V−O1	1× 2.09(2)		

dx.doi.org/10.1021/ic301505e | *Inorg. Chem.* 2012, 51, 11007−11016

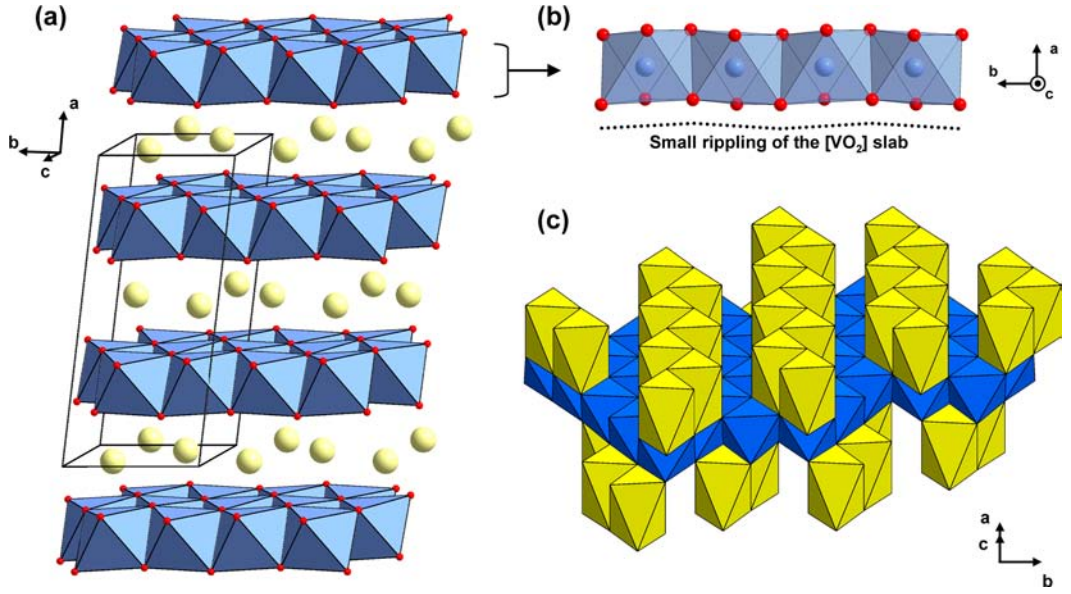

Figure 7. (a) 3D representation of the O′3−$Na_{1/2}VO_2$ layered structure. The full octahedra are VO_6, spheres represent the Na^+ ions. The drawing in (b) highlights the slight rippling of the $[VO_2]$ slab along the b direction. (c) Perspective view showing the position of occupied NaO_6 octahedra (yellow) on each side of a $[VO_2]$ slab (blue).

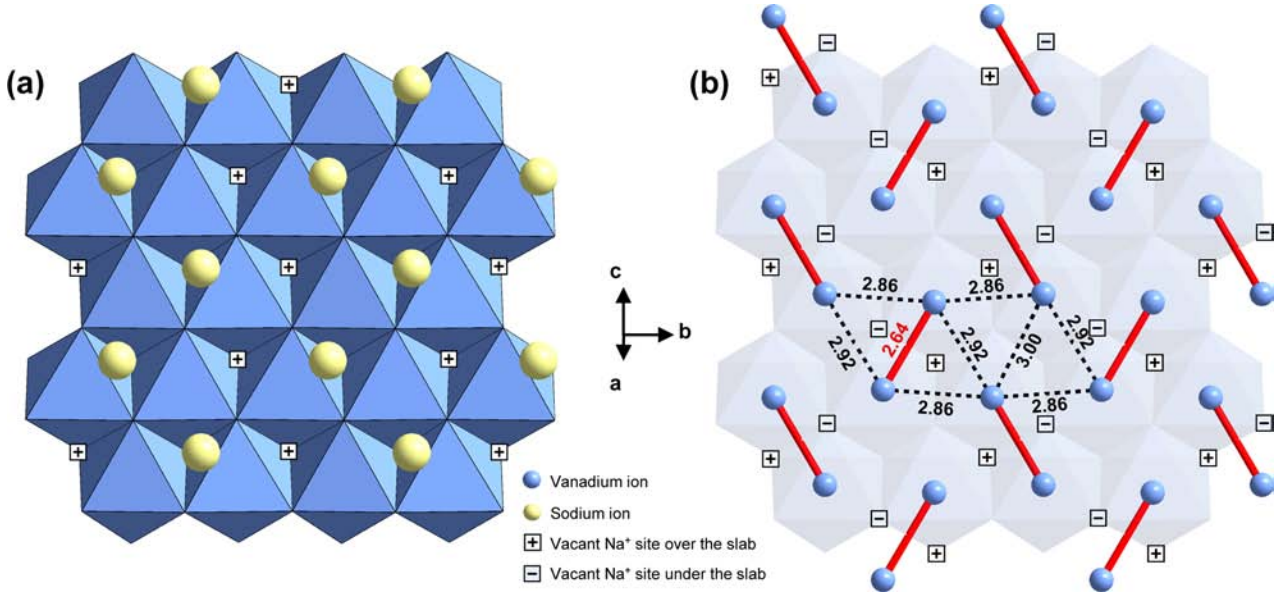

Figure 8. (a) Organization of the Na^+ ions and vacancies in the interslab of O′3−$Na_{1/2}VO_2$. (b) Organization of the V−V distances in a $[VO_2]$ slab. The shortest V−V distance is highlighted in red. Vacant sodium sites on each side of the slab are also represented.

The susceptibility increases for $T < 60$ K (Figure 10) which can be attributed to noncoupled moments. However the value of the susceptibility is low ($\chi = 2.35 \times 10^{-3}$ emu/mol at $T = 2$ K) which means the amount of isolated spins must be very small. One notable feature is the increase of the magnetic susceptibility at higher temperatures ($T \geq 150$ K). At even higher temperatures ($T > 350$ K), it should eventually reach a maximum followed by a Curie−Weiss regime. Unfortunately this observation is not possible as O′3−$Na_{1/2}VO_2$ irreversibly transforms into a P′3 phase[38] at $T \approx 370$ K. This increase of susceptibility is the signature of strong antiferromagnetic interactions which can result from the V−V pairing observed in the structure (Figure 8b and Table 2).

Thus we hypothesize that the magnetism of $Na_{1/2}VO_2$ might be governed by isolated V−V pairs with the vanadium ions coupled antiferromagnetically. From the Rietveld refinement we find only one atomic position for vanadium with a BVS of 3.55(8) hence we assume an equal amount of V^{3+} and V^{4+} on this site. It is well-known that XRD only gives information about long-range ordering; therefore we have no information about the electronic distribution at short-range. Different types of pairs can be considered: an equal mixture of V^{4+}−V^{4+} and V^{3+}−V^{3+} pairs, randomly organized V^{4+}−V^{3+} pairs, or a combination of both hypotheses.

For an antiferromagnetic exchange coupling, the ground state of the first two pairs is a singlet spin state ($S = 0$), while it is a doublet ($S = 1/2$) for the V^{3+}−V^{4+} pair. Consequently the magnetism will be governed by the V^{4+}−V^{3+} pairs at low temperatures. We expect the amount of these pairs to be rather small due to the low value of the susceptibility at low

dx.doi.org/10.1021/ic301505e | Inorg. Chem. 2012, 51, 11007−11016

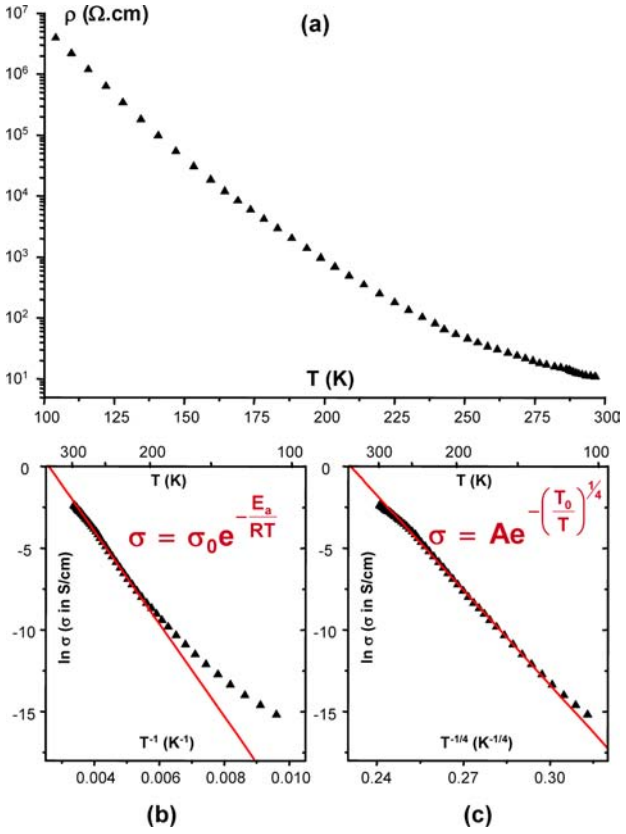

Figure 9. (a) Resistivity measurement made on a pellet of O′3–$Na_{1/2}VO_2$. The insets show the linear regression of ln(σ) with different models: (b) Arrhenius law with a T^{-1} dependence (fitted only in the 297–169 K temperature range, R^2 = 0.9986) and (c) variable range hopping with a $T^{-1/4}$ dependence (fitted in the whole temperature range, R^2 = 0.9983).

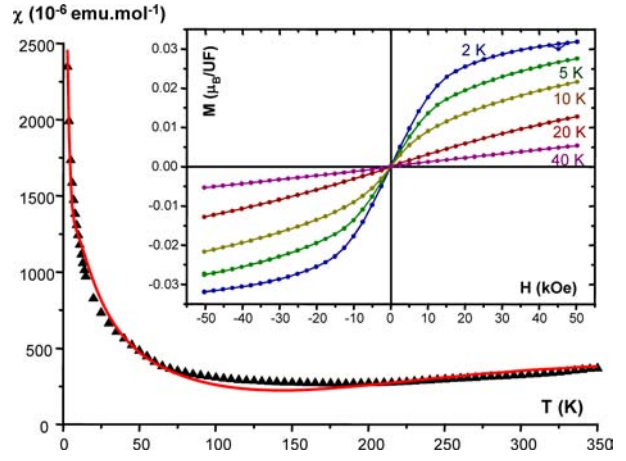

Figure 10. Temperature dependence of the magnetic susceptibility for O′3–$Na_{1/2}VO_2$ powder. The calculated curve of the fit considering V–V pairs is superimposed to the experimental data. The inset shows magnetization measurements versus applied field for different temperatures.

temperatures. As the temperature increases, the susceptibility of the V^{4+}–V^{3+} pairs decreases following a Curie or Curie–Weiss law. Simultaneously the susceptibility of the V^{4+}–V^{4+} and V^{3+}–V^{3+} pairs increases as the excited spin states, which are magnetic, become populated following the Boltzmann distribution. Thus there is a competition between the two

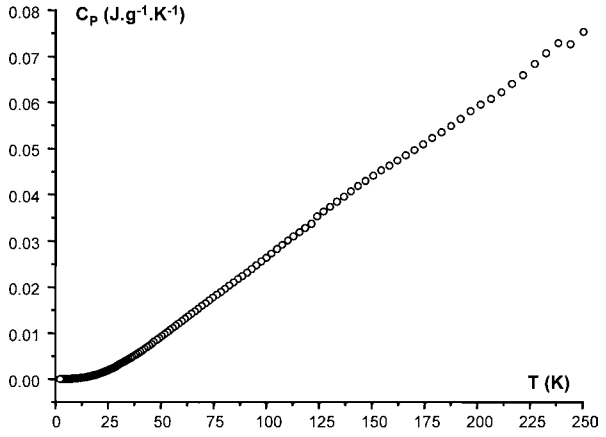

Figure 11. Heat capacity measurements of O′3–$Na_{1/2}VO_2$. The small bumps around 250 K are a contribution from the grease (Apiezon N) used as thermal contact between the sample and the sapphire holder.

magnetic behaviors which leads to a large minimum of the susceptibility, as observed around 150 K (Figure 10). As the contribution of the V^{4+}–V^{4+} and V^{3+}–V^{3+} pairs becomes more and more important, the susceptibility should increase up to a maximum correlated with the strength of the exchange interaction. It is not observed here because the structure transforms irreversibly at $T \approx 370$ K as mentioned above. However the increase of the susceptibility is noticeable up to T = 350 K so there must be a very strong antiferromagnetic exchange coupling within the pairs.

The exchange energy within each pair can be calculated considering the isotropic Heisenberg–Dirac–Van-Vleck (HDVV) Hamiltonian $\hat{H}_{ex.} = -2J_{ij}\ (\hat{s}_i\hat{s}_j)$, where J_{ij} is the intradimer exchange interaction and $\hat{s}_i$ and $\hat{s}_j$ are the spin operators associated with the spins s_i and s_j of the two vanadium atoms within the pair. Let S be the quantum number associated with $\hat{S}$ the total spin operator of a pair, defined as $\hat{S} = \hat{s}_i + \hat{s}_j$; the eigenvalues E_S of $\hat{H}_{ex.}$ can then be obtained with $E_S = -J[S(S+1) - s_i(s_i+1) - s_j(s_j+1)]$. A representation of the spin energy levels for the different pairs is shown in Figure 12. The

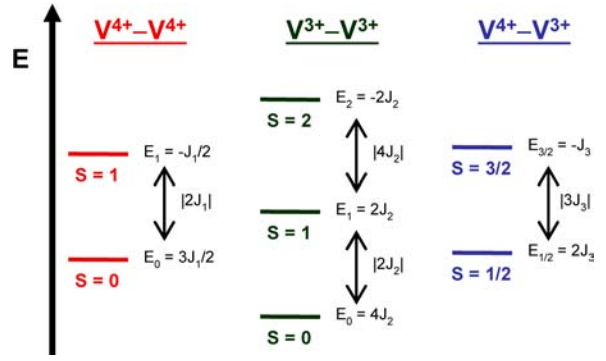

Figure 12. Representation of the spin energy levels of each type of pair of vanadium ions. The relative position of the energy levels between different pairs is unknown. Energy differences are not to scale.

magnetic susceptibility of a pair can be deduced by an average of the different energy levels weighed by their degeneracy and using a Boltzmann statistics, which gives the following equation:

dx.doi.org/10.1021/ic301505e | Inorg. Chem. 2012, 51, 11007–11016

$$\chi_{pair} = g^2 \frac{N_A \mu_B^2}{k_B T} \times \frac{\sum_S \sum_{m_S} m_S^2 \exp(-E_S/k_B T)}{\sum_S (2S+1)\exp(-E_S/k_B T)}$$

where m_S are the eigenvalues of $\hat{S}_z$, the projection of $\hat{S}$ along the z quantification axis.

For the V^{4+}–V^{4+} dimers ($s_i = s_j = 1/2$), with J_1 the exchange coupling energy within the pairs and g_1 the g-factor of the V^{4+} ions, the corresponding susceptibility χ_1 for one pair is

$$\chi_1 = g_1^2 \frac{N_A \mu_B^2}{k_B T} \times \frac{2\exp\left(\frac{1}{2} \times J_1/k_B T\right)}{3\exp\left(\frac{1}{2} \times J_1/k_B T\right) + \exp\left(-\frac{3}{2} \times J_1/k_B T\right)}$$

For the V^{3+}–V^{3+} dimers ($s_i = s_j = 1$), with J_2 the exchange coupling energy within the pairs and g_2 the g-factor of the V^{3+} ions, the corresponding susceptibility χ_2 for one pair is

$$\chi_2 = g_2^2 \frac{N_A \mu_B^2}{k_B T} \times \frac{10\exp(2 \times J_2/k_B T) + 2\exp(-2 \times J_2/k_B T)}{5\exp(2 \times J_2/k_B T) + 3\exp(-2 \times J_2/k_B T) + \exp(-4 \times J_2/k_B T)}$$

In the case of the mixed pairs V^{4+}–V^{3+}, it would be easy to calculate the susceptibility of the pair using the previous procedure if the g-factors were equal. If it is not the case, the matrix is not diagonal in the $|S, m_S\rangle$ basis and therefore the spin states must be expressed in the uncoupled spin states basis $|s_1 m_{s1}, s_2 m_{s2}\rangle$ with $s_1 = 1/2$ and $s_2 = 1$ to calculate the Zeeman effect. The matrix elements were calculated and the susceptibility deduced from the Van-Vleck equation is

$$\chi_3 = \frac{N_A \mu_B^2}{k_B T} \times \frac{A\exp(J_3/k_B T) + B\exp(-2J_3/k_B T)}{4\exp(J_3/k_B T) + 2\exp(-2J_3/k_B T)}$$

$$\text{with } A = \left[\frac{5}{9}(g_1 + 2g_2)^2 + \frac{8}{27}(g_1 - g_2)^2\right]$$

$$\text{and } B = \left[\frac{1}{18}(-g_1 + g_2)^2 - \frac{8}{27}(g_1 - g_2)^2\right]$$

The expression of the magnetic susceptibility of $Na_{1/2}VO_2$ is then

$$\chi = \frac{1}{2}\left[\left(\frac{1-\alpha}{2}\right)\chi_1 + \left(\frac{1-\alpha}{2}\right)\chi_2 + \alpha\chi_3\right]$$

where α is the rate of mixed pairs. The complete expression was least-squares fitted to the experimental data. However high correlations between the different variables led to very large standard deviations in the calculated values. In order to reduce problems of overparameterization, some restrictions were imposed to the procedure. The g-factors of V^{3+} and V^{4+} were considered equal and fixed to $g = 2$. Since the V^{3+}–V^{3+} and V^{4+}–V^{4+} pairs essentially both contribute to the increase of the susceptibility at higher temperatures, strong dependencies were apparent between the J_1 and J_2 parameters (an increase in one was counterbalanced by a decrease in the other). Therefore a crude approximation was made where $J_1 = J_2$.

The fit of the susceptibility is given in Figure 10. The calculated values of the fitted variables are $J_1/k_B = -410(46)$ K, $J_3/k_B = -7.5(4)$ K and $\alpha = 0.039(4)°$. As expected the exchange coupling within the V^{4+}–V^{4+} and V^{3+}–V^{3+} pairs is strongly antiferromagnetic ($J_1 \ll 0$). The fit only converged when the rate α of mixed pairs V^{4+}–V^{3+} was very small, as expected by the low value of the susceptibility. However one cannot exclude that the increase of the susceptibility at $T < 60$ K results from a small paramagnetic impurity or isolated V^{3+}/V^{4+} species at grain boundaries. Nevertheless one can conclude that the magnetism of O′3–$Na_{1/2}VO_2$ at $T > 150$ K is mainly governed by strongly antiferromagnetic pairs (V^{4+}–V^{4+} and V^{3+}–V^{3+}) with a singlet spin ground-state. This result is in agreement with the presence of only one crystallographic site for vanadium (Table 1).

CONCLUSION

The in situ measurement shows the strong relationship between the electrochemical curve (Fermi level vs Na^+/Na) and the phase transitions. For O′3–Na_xVO_2, it allowed us to identify different compositions where single phases could be obtained. Using electrochemistry, we synthesized O′3–$Na_{1/2}VO_2$, for which there is a superstructure due to a Na^+/vacancy ordering, associated with a pairing of vanadium atoms. The ordering of sodium ions within the interslab is a result of the minimization of the electrostatic repulsions. However the pairing of the transition metal element in layered oxides was not observed before and seems to be specific to vanadium. First measurements of the physical properties have been made and an explanation of the magnetic behavior is proposed based on a strong V–V pairing in the structure. This shows the structure/properties correlations in this family of materials. The sodium–vanadium layered oxides are interesting from the physical point of view, as was already demonstrated for $NaVO_2$,[8,32−34] this paper shows that the deintercalated species might also present interesting features. This work will be extended to physical properties characterization of other Na_xVO_2 compositions, such as $Na_{2/3}VO_2$ or the observed solid solution around $Na_{\sim 0.63}VO_2$.

ASSOCIATED CONTENT

Supporting Information

Tables of the refined atomic parameters and interatomic distances from the Rietveld refinement of O′3–$Na_{1/2}VO_2$ obtained with XRD at 10 K and pattern indexation obtained with ND at various temperatures. This material is available free of charge via the Internet at http://pubs.acs.org.

AUTHOR INFORMATION

Corresponding Author

*E-mail: delmas@icmcb-bordeaux.cnrs.fr.

Author Contributions

The manuscript was written through contributions of all authors.

Funding

This work was supported by the Centre National de la Recherche Scientifique (CNRS) and Université de Bordeaux.

Notes

The authors declare no competing financial interest.

ACKNOWLEDGMENTS

The authors wish to thank Gilles André and Françoise Damay of Laboratoire Léon Brillouin (Saclay, France) for their help during neutron diffraction acquisitions.

REFERENCES

(1) Komaba, S.; Takei, C.; Nakayama, T.; Ogata, A.; Yabuuchi, N. *Electrochem. Commun.* **2010**, *12*, 355–358.

(2) Ma, X.; Chen, H.; Ceder, G. *J. Electrochem. Soc.* **2011**, *158*, A1307−A1312.
(3) Xia, X.; Dahn, J. *Electrochem. Solid State* **2012**, *15*, A1−A4.
(4) Yabuuchi, N.; Kajiyama, M.; Iwatate, J.; Nishikawa, H.; Hitomi, S.; Okuyama, R.; Usui, R.; Yamada, Y.; Komaba, S. *Nat. Mater.* **2012**, DOI: 10.1038/nmat3309.
(5) Komaba, S.; Yabuuchi, N.; Nakayama, T.; Ogata, A.; Ishikawa, T.; Nakai, I. *Inorg. Chem.* **2012**, *51*, 6211−6220.
(6) Clarke, S.; Fowkes, A.; Harrison, A.; Ibberson, R.; Rosseinsky, M. *Chem. Mater.* **1998**, *10*, 372−384.
(7) Takada, K.; Sakurai, H.; Takayama-Muromachi, E.; Izumi, F.; Dilanian, R.; Sasaki, T. *Nature* **2003**, *422*, 53−55.
(8) Onoda, M. *J. Phys.: Condens. Matter* **2008**, *20*, 145205.
(9) Dyer, L.; Borie, B., Jr.; Smith, G. *J. Am. Chem. Soc.* **1954**, *76*, 1499−1503.
(10) Parant, J.-P.; Olazcuaga, R.; Devalette, M.; Fouassier, C.; Hagenmuller, P. *J. Solid State Chem.* **1971**, *3*, 1−11.
(11) Fouassier, C.; Matejka, G.; Reau, J.-M.; Hagenmuller, P. *J. Solid State Chem.* **1973**, *6*, 532−537.
(12) Barker, M.; Hooper, A. *J. Chem. Soc. Dalton* **1973**, 1517−1519.
(13) Braconnier, J. .; Delmas, C.; Fouassier, C.; Hagenmuller, P. *Mater. Res. Bull.* **1980**, *15*, 1797−1804.
(14) Miyazaki, S.; Kikkawa, S.; Koizumi, M. *Synth. Met.* **1983**, *6*, 211−217.
(15) Maazaz, A.; Delmas, C.; Hagenmuller, P. *J. Inclusion Phenom.* **1983**, *1*, 45−51.
(16) Terasaki, I.; Sasago, Y.; Uchinokura, K. *Phys. Rev. B Condens. Matter Mater. Phys.* **1997**, *56*, 50.
(17) Huang, Q.; Foo, M.; Pascal, J.; Lynn, J.; Toby, B.; He, T.; Zandbergen, H.; Cava, R. *Phys. Rev. B Condens. Matter Mater. Phys.* **2004**, *70*, 1−7.
(18) Foo, M.; Wang, Y.; Watauchi, S.; Zandbergen, H.; He, T.; Cava, R.; Ong, N. *Phys. Rev. Lett.* **2004**, *92*, 247001−1.
(19) Viciu, L.; Bos, J.; Zandbergen, H.; Huang, Q.; Foo, M.; Ishiwata, S. d.; Ramirez, A.; Lee, M.; Ong, N.; Cava, R. *Phys. Rev. B Condens. Matter Mater. Phys.* **2006**, *73*, 174104.
(20) Berthelot, R.; Carlier, D.; Delmas, C. *Nat. Mater.* **2011**, *10*, 74−80.
(21) Roger, M.; Morris, D.; Tennant, D. d.; Gutmann, M.; Goff, J.; Hoffmann, J.-U.; Feyerherm, R.; Dudzik, E.; Prabhakaran, D.; Boothroyd, A.; Shannon, N.; Lake, B. d.; Deen, P. *Nature* **2007**, *445*, 631−634.
(22) Delmas, C.; Braconnier, J.-J.; Maazaz, A.; Hagenmuller, P. *Rev. Chim. Miner.* **1982**, *19*, 343.
(23) Zandbergen, H.; Foo, M.; Xu, Q.; Kumar, V.; Cava, R. *Phys. Rev. B Condens. Matter Mater. Phys.* **2004**, *70*, 024101−1.
(24) Huang, F.-T.; Chu, M.-W.; Shu, G.; Sheu, H.; Chen, C.; Liu, L.-K.; Lee, P.; Chou, F. *Phys. Rev. B Condens. Matter Mater. Phys.* **2009**, *79*, 014413.
(25) Alloul, H.; Mukhamedshin, I.; Platova, T.; Dooglav, A. *Europhys. Lett.* **2009**, *85*, 47006.
(26) Foury-Leylekian, P.; Poltavets, V.; Jaouen, N.; Rueff, J.-P. d.; Lorenzo, J.; Auban-Senzier, P.; Pasquier, C.; Mazzoli, C.; Greenblatt, M. *Phys. Rev. B Condens. Matter Mater. Phys.* **2009**, 79.
(27) Williams, A.; Attfield, J.; Foo, M.; Viciu, L.; Cava, R. *Phys. Rev. B Condens. Matter Mater. Phys.* **2006**, *73*, 1−5.
(28) Huang, Q.; Foo, M.; Lynn, J.; Zandbergen, H.; Lawes, G.; Wang, Y.; Toby, B.; Ramirez, A.; Ong, R.; N.P.; Cava. *J. Phys.: Condens. Matter* **2004**, *16*, 5803−5814.
(29) Wang, N.; Wu, D.; Li, G.; Chen, X.; Wang, C.; Luo, X. *Phys. Rev. Lett.* **2004**, *93*, 147403−1.
(30) Bobroff, J.; Lang, G.; Alloul, H.; Blanchard, N.; Collin, G. *Phys. Rev. Lett.* **2006**, *96*, 1−4.
(31) Chamberland, B.; Porter, S. *J. Solid State Chem.* **1988**, *73*, 398−404.
(32) McQueen, T.; Stephens, P.; Huang, Q.; Klimczuk, T. e.; Ronning, F.; Cava, R. *Phys. Rev. Lett.* **2008**, *101*, 166402.
(33) Jia, T.; Zhang, G.; Zeng, Z.; Lin, H. *Phys. Rev. B Condens. Matter Mater. Phys.* **2009**, *80*, 045103.
(34) Ouyang, Z.; Xia, N.; Sheng, S.; Chen, J.; Xia, Z.; Rao, G.; Zheng, X. *Phys. Rev. B Condens. Matter Mater. Phys.* **2011**, *83*, 094417.
(35) Chou, F.; Abel, E.; Cho, J.; Lee, Y. *J. Phys. Chem. Solids* **2005**, *66*, 155−160.
(36) Didier, C.; Guignard, M.; Denage, C.; Szajwaj, O.; Ito, S.; Saadoune, I.; Darriet, J.; Delmas, C. *Electrochem. Solid State* **2011**, *14*, A75−A78.
(37) Hamani, D.; Ati, M.; Tarascon, J.-M.; Rozier, P. *Electrochem. Commun.* **2011**, *13*, 938−941.
(38) Szajwaj, O.; Gaudin, E.; Weill, F.; Dariet, J.; Delmas, C. *Inorg. Chem.* **2009**, *48*, 4197.
(39) Petricek, V.; Dusek, M.; Palatinus, M. *JANA2006_The crystallographic computing system*, 2006, Institute of Physics, Praha, Czech Republic.
(40) Thompson, P.; Cox, D. E.; Hastings, J. B. *J. Appl. Crystallogr.* **1987**, *20*, 79−83.
(41) Bain, G. A.; Berry, J. F. *J. Chem. Educ.* **2008**, *85*, 532−null.
(42) Palatinus, L. *Acta Crystallogr.* **2004**, *A60*, 451−456.
(43) Pitschke, W.; Hermann, H.; Mattern, N. *J. Appl. Crystallogr.* **1993**, *26*, 132−134.
(44) Longo, J.; Kierkegaard, P. *Acta Chem. Scand.* **1970**, *24*, 420−426.
(45) Le Page, Y.; Bordet, P.; Marezio, M. *J. Solid State Chem.* **1991**, *92*, 380−385.
(46) Marezio, M.; McWhan, D.; Dernier, P.; Remeika, J. *J. Solid State Chem.* **1973**, *6*, 419−429.
(47) Dernier, P. *J. Phys. Chem. Solids* **1970**, *31*, 2569−2575.
(48) Mott, N. F. *Philos. Mag.* **1969**, *19*, 835−852.
(49) Mott, N.; Davis, E. *Electronic Processes in Non Crystalline Materials*; Clarendon: Oxford, U.K., 1979.